This article has been accepted for publication in Journal of Lightwave Technology. This is the author's version which has not been fully edited and content may change prior to final publication. Citation information: DOI 10.1109/JLT.2026.3745673

Stokes-Derived Rotation Descriptor for Long-Haul Forward-Transmission Distributed Fiber-Optic Sensing

Xing Rao, Yiping Wang, Senior IEEE Member, and George Y. Chen, Senior IEEE Member

***Abstract*—Forward-transmission fiber-optic distributed sensing is attractive for reusing long-haul telecommunication fibers as environmental monitoring links, but direct interpretation of the state of polarization (SOP) is complicated by random birefringence, launch polarization state, wavelength-dependent polarization transfer, and slow polarization drift. This work employs a scalar Stokes rotation-rate descriptor that characterizes the instantaneous angular speed of the measured SOP trajectory on the Poincaré sphere, rather than relying directly on individual Stokes components or absolute SOP coordinates. The method is experimentally demonstrated over a 202.1 km standard single-mode fiber link using synchronized dual-end SOP measurements. The experiments with six representative launch SOPs show that the proposed descriptor exhibits an across-state coefficient of variation of 17.01%, compared with 61.46%–117.92% for the conventional polarization observables, together with more consistent detection SNR across launch states. The extracted rotation-rate waveform further enables sub-0.5 km single-event localization over the five tested positions, while frequency-separated dual-event detection is demonstrated as a proof of concept. These results establish the Stokes rotation rate as a compact and comparatively launch-SOP-consistent observable for dynamic perturbation sensing over long-haul forward-transmission fiber links.**

***Index Terms*—Forward DAS, State of polarization, Stokes-domain rotation descriptor.**

I. INTRODUCTION

Long-haul optical fiber links provide not only high-capacity communication channels but also widely deployed guided-wave infrastructures for environmental sensing [1-3]. External perturbations such as vibration, strain, acoustic excitation, and mechanical disturbance can modify the phase [4], intensity [5], and state of polarization [6] of the transmitted optical field. By monitoring these transmission-domain variations at the receiving terminals, forward-transmission distributed fiber-optic sensing can potentially reuse existing fiber links without relying on distributed backscattering interrogation [7-9]. This feature is particularly attractive for long-haul telecommunication fibers and submarine or intercity cable systems, where access to intermediate fiber sections is limited and backscatter-based interrogation may suffer from severe attenuation over long distances [10].

Conventional distributed fiber-optic sensing systems, including phase-sensitive optical time-domain reflectometry and related backscattering-based approaches, have achieved high sensitivity and fine spatial resolution [11, 12]. However, these systems usually require dedicated interrogation units and high-power probing pulses [13]. For long-haul communication links, especially those already carrying data traffic, it is often desirable to extract sensing information from the transmitted optical field itself. In this context, forward-transmission sensing methods offer a complementary route: the perturbation is detected through the accumulated changes of the received optical field, rather than through weak backscattered signals [14].

Among different transmission-domain observables, the state of polarization is highly sensitive to external perturbations since local stress, bending, vibration, and temperature variation can change the birefringence and coupling characteristics of the fiber itself [15, 16]. However, this high sensitivity also makes SOP-based sensing difficult to interpret over long distances. The received SOP is affected not only by the local perturbation but also by the accumulated random birefringence along the entire link, the launched polarization state, wavelength-dependent polarization transfer, and slow environmental drift [17]. As a result, direct use of individual Stokes components often leads to coordinate-dependent and drift-sensitive responses, which limits the robustness of SOP-based forward-transmission sensing [15, 18].

A more fundamental difficulty arises from the observability of polarization evolution itself. From a single terminal Stokes trajectory, only the component of the polarization generator perpendicular to the instantaneous Stokes vector contributes to the measured SOP variation, whereas the parallel component remains unobservable. Moreover, in a long-haul link, a localized perturbation is embedded between different accumulated polarization transformations before and after the perturbed section. Consequently, the measured terminal SOP trajectory depends not only on the local perturbation but also on perturbation position, operating wavelength, and launch SOP. These effects make it difficult to directly interpret the measured

The work is supported by National Natural Science Foundation of China (W2532046, 62275172, U22A2088); Shenzhen Science and Technology Program (JCYJ20241202124408012, JCYJ20220818095800001); Shenzhen Key Laboratory of Ultrafast Laser Micro/Nano Manufacturing (ZDSYS20220606100405013); Research Team Cultivation Program of Shenzhen University (2023DFT001). (*Corresponding author: George Y. Chen*)

Xing Rao, George Y. Chen and Yiping Wang are with State Key Laboratory of Radio Frequency Heterogeneous Integration, Key Laboratory of Optoelectronic Devices and Systems of Ministry of Education/Guangdong Province, College of Physics and Optoelectronic Engineering, Shenzhen University, Shenzhen 518060, China. Shenzhen Key Laboratory of Ultrafast Laser Micro/Nano Manufacturing, Guangdong and Hong Kong Joint Research Centre for Optical Fibre Sensors, Shenzhen University, Shenzhen 518060, China. (e-mail: raoxing@szu.edu.cn; gychen@szu.edu.cn; ypwang@szu.edu.cn)

Authorized licensed use limited to: SHENZHEN UNIVERSITY. Downloaded on October 23,2026 at 04:14:54 UTC from IEEE Xplore. Restrictions apply.
© 2026 IEEE. All rights reserved, including rights for text and data mining and training of artificial intelligence and similar technologies. Personal use is permitted, but republication/redistribution requires IEEE permission. See https://www.ieee.org/publications/rights/index.html for more information.

This article has been accepted for publication in Journal of Lightwave Technology. This is the author's version which has not been fully edited and content may change prior to final publication. Citation information: DOI 10.1109/JLT.2026.3745673

terminal response in terms of unique microscopic coupling or birefringence parameters.

To address this observability limitation, this work adopts a kinematic description of the measured SOP evolution and employs a scalar Stokes rotation-rate descriptor, defined as the instantaneous angular speed of the normalized Stokes trajectory on the Poincaré sphere. Rather than relying on the absolute position of the SOP or on individual Stokes projections, the descriptor characterizes the temporal rate of the complete polarization trajectory. Its magnitude is invariant to a static rotation of the Stokes observation coordinates, while its physical dependence on the launch SOP is treated explicitly as an experimental robustness characteristic rather than as an intrinsic invariance. This representation is therefore intended to provide a compact and comparatively launch-SOP-consistent observable for dynamic perturbation sensing.

II. Principles of Stokes-Derived Rotation Descriptors

In this section, the Stokes-domain representation used for the subsequent sensing analysis is introduced. The purpose of the following formulation is to establish the relationship between perturbation-induced polarization evolution in Jones space and the experimentally observable rotation of the Stokes vector on the Poincaré sphere. Particular attention is given to the observability of the polarization generator from a single terminal Stokes trajectory. Rather than attempting to reconstruct the complete microscopic Jones operator or the full local polarization generator of the perturbed fiber segment, which are generally not identifiable from terminal SOP measurements alone, this work focuses on the observable rotation component inferred from the measured Stokes evolution. Based on this observable component, a scalar rotation-rate descriptor in the terminal Stokes observation basis are subsequently defined for sensing analysis, as illustrated in Fig. 1.

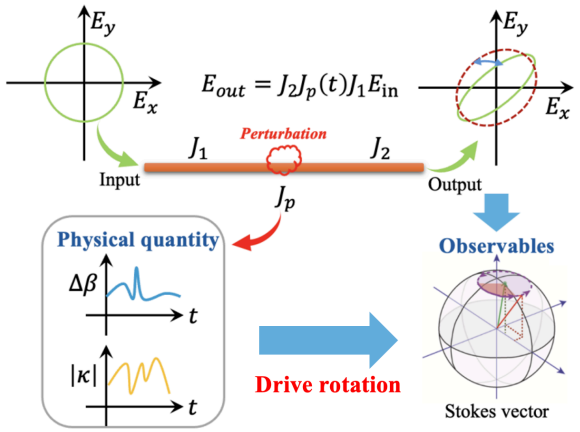


Fig. 1. Illustration of operator-based interpretation of polarization-based perturbation sensing.

The coupled-mode description and the Jones/Stokes rotation relation used below follow the standard formulation of polarization evolution in birefringent optical fibers and the SU(2)-to-SO(3) mapping between Jones space and the Poincaré sphere [19-21]. They are introduced here to establish the notation and physical basis required for deriving the experimentally observable Stokes-domain rotation descriptors. When an optical field propagates through a single-mode fiber (SMF), its SOP can be represented as a superposition of two orthogonal polarization modes. Denote the slowly varying Jones vector of the forward-propagating field in a fixed orthonormal polarization basis as [19]:

$$\boldsymbol{A}(z) = \begin{bmatrix} A_x(z) \\ A_y(z) \end{bmatrix} \tag{1}$$

where $A_x(z)$ and $A_y(z)$ are the complex envelopes of the two orthogonal polarization components. External perturbations (e.g., strain or vibration) modify the local birefringence and polarization coupling in the fiber. Under the weak-guidance approximation and neglecting loss over the perturbed segment, the field evolution can be described by the coupled-mode equation [19]:

$$\frac{d\boldsymbol{A}(z)}{dz} = i\boldsymbol{H}(z) \cdot \boldsymbol{A}(z) \tag{2}$$

where $\boldsymbol{H}(z)$ is a Hermitian 2×2 matrix describing the local polarization coupling. In the lossless case, it can be written as [20]:

$$\boldsymbol{H}(\boldsymbol{z}) = \begin{bmatrix} \beta_x(z) & \kappa(z) \\ \kappa^*(z) & \beta_y(z) \end{bmatrix} \tag{3}$$

where $\beta_x(z)$ and $\beta_y(z)$ are the local propagation constants, $\Delta\beta(z) = \beta_x(z) - \beta_y(z)$ is the local birefringence-induced phase mismatch, and $\kappa(z)$ is the complex coupling coefficient. To remove the common (global) phase accumulation, define $\bar{\beta}(z) = [\beta_x(z) + \beta_y(z)]/2$ and apply $\boldsymbol{A}(z) = e^{i\int \bar{\beta}(z)dz}\boldsymbol{A}'(z)$, Eq. 2 and Eq. 3 can be rewritten as [20]:

$$\frac{d\boldsymbol{A}'(z)}{dz} = i\boldsymbol{H}'(z) \cdot \boldsymbol{A}'(z)$$

$$\boldsymbol{H}'(z) = \begin{bmatrix} \dfrac{\Delta\beta(z)}{2} & \kappa(z) \\ \kappa^*(z) & -\dfrac{\Delta\beta(z)}{2} \end{bmatrix} \tag{4}$$

Since the common phase term does not affect the SOP, only the traceless part $\boldsymbol{H}'(z)$ is relevant to the polarization rotation considered below. Any traceless Hermitian 2×2 matrix can be expanded on the Pauli basis. Using the Pauli matrices $\sigma_x = \begin{bmatrix} 0 & 1 \\ 1 & 0 \end{bmatrix}, \sigma_y = \begin{bmatrix} 0 & -i \\ i & 0 \end{bmatrix}, \sigma_z = \begin{bmatrix} 1 & 0 \\ 0 & -1 \end{bmatrix}$ and the Pauli vector $\boldsymbol{\sigma} = [\sigma_x,\ \sigma_y,\ \sigma_z]^T$, the original equation can be written in a more compact form [21]:

$$\boldsymbol{H}'(z) = \boldsymbol{\Omega}(z) \cdot \boldsymbol{\sigma} \tag{5}$$

Writing the complex coupling coefficient as $\kappa(z) = \kappa_r(z) + i\kappa_i(z)$, the generator vector $\boldsymbol{\Omega}(z) = [\Omega_x(z),\ \Omega_y(z),\ \Omega_z(z)]^T$ can be represented as [20]:

$$\Omega_x(z) = \kappa_r(z), \Omega_y(z) = -\kappa_i(z), \Omega_z(z) = \frac{\Delta\beta(z)}{2} \tag{6}$$

It is important to clarify the coordinate system associated with Eq. 6. The three components of $\boldsymbol{\Omega}$ refer to the Pauli coordinates associated with the selected Jones basis and, equivalently, to the corresponding coordinate axes of the Poincaré sphere. They should not be interpreted as fixed Cartesian directions of the physical fiber. Accordingly, the decomposition of $\boldsymbol{\Omega}$ into its three components is basis dependent. Under a change of polarization basis, the generator

Authorized licensed use limited to: SHENZHEN UNIVERSITY. Downloaded on October 23,2026 at 04:14:54 UTC from IEEE Xplore. Restrictions apply.
© 2026 IEEE. All rights reserved, including rights for text and data mining and training of artificial intelligence and similar technologies. Personal use is permitted, but republication/redistribution requires IEEE permission. See https://www.ieee.org/publications/rights/index.html for more information.

This article has been accepted for publication in Journal of Lightwave Technology. This is the author's version which has not been fully edited and content may change prior to final publication. Citation information: DOI 10.1109/JLT.2026.3745673

vector undergoes the corresponding rotation in Stokes space, while its Euclidean magnitude is preserved. Recovering the generator components in the local principal-axis basis of a perturbed fiber section would require knowledge of the corresponding Jones transformation or additional independent polarization measurements. Such information is not available from a single terminal Stokes trajectory in the present experiment. Therefore, although Eq. 6 establishes the physical meaning of the complete generator in a specified Jones basis, its individual components are not treated as independently measurable sensing quantities in this work. The SOP can be equivalently represented by the normalized Stokes vector on the Poincaré sphere $\boldsymbol{S}(\mathrm{z})$. Using the global-phase definition [21]:

$$\boldsymbol{S}(\mathrm{z}) = \frac{\boldsymbol{A}'^{\dagger}(z)\boldsymbol{\sigma}\boldsymbol{A}'(z)}{\boldsymbol{A}'^{\dagger}(z)\boldsymbol{A}'(z)} \in \mathbb{R}^{\mathbf{3}}, \qquad \|\boldsymbol{S}(\mathrm{z})\| = 1 \tag{7}$$

where $\boldsymbol{A}'^{\dagger}(z)$ is the conjugate of $\boldsymbol{A}'(z)$. One obtains, by differentiating Eq.7 and using Eq.4-6 [20]:

$$\frac{d\boldsymbol{S}(\mathrm{z})}{dz} = -2\boldsymbol{\Omega}(\mathrm{z}) \times \boldsymbol{S}(\mathrm{z}) \tag{8}$$

Eq. 8 describes the local Stokes-space rotation generated by the physical polarization generator $\boldsymbol{\Omega}$. However, it is essential to distinguish the physical generator from the part of it that is observable from a single Stokes trajectory. Taking the cross product of $\boldsymbol{S}$ with both sides of Eq. (8) and using $\|\boldsymbol{S}\| = 1$ gives:

$$-\frac{1}{2}\boldsymbol{S} \times \frac{d\boldsymbol{S}}{dz} = \boldsymbol{S} \times (\boldsymbol{\Omega} \times \boldsymbol{S}) = \boldsymbol{\Omega} - (\boldsymbol{\Omega} \cdot \boldsymbol{S})\boldsymbol{S} \tag{9}$$

We therefore define:

$$\boldsymbol{\Omega}_{\perp} = \boldsymbol{\Omega} - (\boldsymbol{\Omega} \cdot \boldsymbol{S})\boldsymbol{S} \tag{10}$$

which is the component of the physical generator perpendicular to the instantaneous Stokes vector. The complete generator can be decomposed as:

$$\begin{aligned} \boldsymbol{\Omega} &= \boldsymbol{\Omega}_{\perp} + \boldsymbol{\Omega}_{\parallel} \\ \boldsymbol{\Omega}_{\parallel} &= (\boldsymbol{\Omega} \cdot \boldsymbol{S})\boldsymbol{S} \end{aligned} \tag{11}$$

The parallel component $\boldsymbol{\Omega}_{\parallel}$ does not contribute to $d\boldsymbol{S}/dz$, since $\boldsymbol{\Omega}_{\parallel} \times \boldsymbol{S} = \boldsymbol{0}$. It is therefore unobservable from the instantaneous evolution of a single Stokes vector. Consequently, the measured Stokes trajectory determines only $\boldsymbol{\Omega}_{\perp}$, whereas an arbitrary component parallel to $\boldsymbol{S}$ can be added without changing the observed trajectory. A single Stokes trajectory is thus insufficient to uniquely reconstruct the complete physical generator $\boldsymbol{\Omega}$. Among the family of generators consistent with the same instantaneous Stokes evolution, $\boldsymbol{\Omega}_{\perp}$ has the minimum Euclidean norm since its unobservable parallel component is zero. It can therefore be interpreted as the minimum-rotation generator consistent with the observed trajectory:

$$\boldsymbol{\Omega}_{min} = \boldsymbol{\Omega}_{\perp} = -\frac{1}{2}\boldsymbol{S} \times \frac{d\boldsymbol{S}}{dz} \tag{12}$$

This quantity should be distinguished from the complete physical generator. Consequently, the Cartesian components of $\boldsymbol{\Omega}_{min}$ should be regarded as observation-basis descriptors and, in general, cannot be uniquely identified with the microscopic polarization-coupling coefficient or differential propagation constant of the fiber. A direct consequence of Eq. 12 is that when the physical generator is locally parallel to the Stokes vector, $\boldsymbol{\Omega} \parallel \boldsymbol{S}$, the measured first-order Stokes variation vanishes even when $\|\boldsymbol{\Omega}\| \neq \boldsymbol{0}$. This represents an intrinsic observability limitation of any sensing method based on a single instantaneous SOP trajectory. The proposed descriptors therefore characterize the observable polarization dynamics rather than the complete underlying polarization transformation.

For a localized perturbation embedded in a long-haul fiber link, the terminal polarization response additionally depends on the fiber sections surrounding the perturbation. The corresponding end-to-end Jones transformation can be conceptually factorized as:

$$\boldsymbol{J}_{tot} = \boldsymbol{J}_2\boldsymbol{J}_p\boldsymbol{J}_1 \tag{13}$$

where $\boldsymbol{J}_p$ represents the polarization transformation associated with the perturbed section, while $\boldsymbol{J}_1$ and $\boldsymbol{J}_2$ represent the accumulated polarization transformations before and after that section, respectively. Eq. 13 introduces an additional observation dependence in a long-haul transmission link. Even for the same local perturbation, the corresponding terminal Stokes trajectory can vary with perturbation position, operating wavelength, and launched SOP since the perturbation-induced polarization change is mapped through different accumulated fiber transformations before reaching the observation terminal. Therefore, the absolute orientation and amplitude of the measured Stokes response should not be interpreted as direct measurements of the microscopic perturbation generator.

The preceding spatial formulation describes how polarization evolves along the fiber and establishes the observability limit of the underlying polarization generator. In the experiment, however, the polarization analyzer is fixed at the receiving terminal and records the time-dependent terminal Stokes vector $\boldsymbol{S}_{rx}(t) = \boldsymbol{S}(z_{rx}, t)$. The experimentally accessible sensing signal is therefore the temporal trajectory of the terminal SOP rather than its spatial derivative along the fiber. Since $\|\boldsymbol{S}_{rx}(t)\| = 1$, its instantaneous temporal derivative lies in the tangent plane of the Poincaré sphere and can always be represented kinematically as:

$$\frac{d\boldsymbol{S}_{rx}(t)}{dt} = \boldsymbol{\omega}(t) \times \boldsymbol{S}_{rx}(t) \tag{14}$$

Here, $\boldsymbol{\omega}(t)$ is an effective temporal angular-velocity vector, with units of rad/s, defined directly through Eq. 14. It differs from the spatial generator $\boldsymbol{\Omega}(\mathrm{z})$, which is defined through the Pauli expansion of the Jones evolution operator in Eq. 5. The factor of two in the spatial Stokes evolution follows from the Pauli-matrix commutation relations, whereas no additional factor is required in Eq. 14 since $\boldsymbol{\omega}(t)$ directly represents the Stokes-space angular velocity. The spatial and temporal quantities therefore have different definitions and units. Eq. 14 does not establish a conversion from the local spatial generator to the measured terminal dynamics. The minimum-norm rotation vector consistent with the observed trajectory is therefore:

$$\boldsymbol{\omega}_{obs}(t) = \boldsymbol{S}_{rx}(t) \times \frac{d\boldsymbol{S}_{rx}(t)}{dt} \tag{15}$$

In the present work, no component-wise decomposition of $\boldsymbol{\omega}_{\boldsymbol{obs}}(t)$ is used. Instead, only its magnitude is retained as a scalar measure of the temporal polarization dynamics. We define the Stokes rotation-rate descriptor as:

$$\omega_{rot}(t) = \|\boldsymbol{\omega}_{obs}(t)\| = \left\|\boldsymbol{S}_{\boldsymbol{rx}}(t) \times \frac{d\boldsymbol{S}_{\boldsymbol{rx}}(t)}{dt}\right\| \tag{16}$$

Authorized licensed use limited to: SHENZHEN UNIVERSITY. Downloaded on October 23,2026 at 04:14:54 UTC from IEEE Xplore. Restrictions apply.
© 2026 IEEE. All rights reserved, including rights for text and data mining and training of artificial intelligence and similar technologies. Personal use is permitted, but republication/redistribution requires IEEE permission. See https://www.ieee.org/publications/rights/index.html for more information.

This article has been accepted for publication in Journal of Lightwave Technology. This is the author's version which has not been fully edited and content may change prior to final publication. Citation information: DOI 10.1109/JLT.2026.3745673

Since the normalized Stokes vector satisfies $\boldsymbol{S}(t) \cdot \boldsymbol{S}(t) = 1$, differentiation with respect to time gives $\boldsymbol{S}(t) \cdot \boldsymbol{S}(t)/dt = 0$. Therefore,

$$\omega_{rot}(t) = \left\| \frac{d\boldsymbol{S}(t)}{dt} \right\| \tag{17}$$

Thus, $\omega_{rot}(t)$ represents the instantaneous angular speed of the measured SOP trajectory on the unit Poincaré sphere. It quantifies the temporal strength of the observable polarization variation without assigning the measured response to individual microscopic coupling or birefringence parameters. This scalar quantity is therefore used as the sensing descriptor throughout the remainder of this work.

An important property of $\omega_{rot}(t)$ is its invariance to a static rotation of the Stokes coordinate system. Consider the same physical Stokes trajectory represented in another polarization basis by:

$$\boldsymbol{S}'(t) = \boldsymbol{R}\boldsymbol{S}(t), \boldsymbol{R} \in SO(3) \tag{18}$$

where $\boldsymbol{R}$ is a time-independent rotation matrix. Since a rotation matrix preserves the Euclidean norm:

$$\omega'_{rot}(t) = \left\| \frac{d\boldsymbol{S}'_{rot}(t)}{dt} \right\| = \left\| \frac{d\boldsymbol{S}(t)}{dt} \right\| = \omega_{rot}(t) \tag{19}$$

Thus, although the individual Stokes components depend on the chosen observation basis, the scalar rotation rate remains unchanged when the same physical SOP trajectory is expressed in a different, time-independent polarization basis. This coordinate invariance does not imply invariance to changes in the physical launch SOP or to time-varying polarization drift.

It should be emphasized, however, that coordinate invariance does not imply invariance to a physical change of the launched SOP. From Eq. 14, the magnitude of the observable response depends on the relative orientation between the instantaneous Stokes vector and the effective rotation axis. When their directions approach parallel alignment, the observable Stokes variation can decrease substantially and may vanish in the limiting case. Similarly, a time-varying background polarization transformation can itself contribute to $d\boldsymbol{S}/dt$. Therefore, launched-SOP dependence and slow polarization drift are treated in this work as experimental robustness characteristics rather than intrinsic mathematical invariances of the rotation-rate descriptor.

In summary, the coupled-mode formulation establishes the physical origin of perturbation-induced polarization evolution, while the Stokes-space analysis identifies the part of this evolution that is accessible from terminal SOP measurements. A single Stokes trajectory cannot uniquely reconstruct the complete microscopic polarization generator, and the accumulated transformations of a long-haul fiber further map the local perturbation into a terminal response that depends on the propagation path and operating condition. The present method therefore does not attempt to recover microscopic coupling or birefringence parameters. Instead, the scalar Stokes rotation rate $\omega_{rot}(t)$ is used as the sole descriptor of the measured polarization dynamics for subsequent perturbation characterization and dual-end delay localization.

III. Experiment Setup

The experimental configuration for long-haul forward-transmission polarization sensing is shown in Fig. 2. A 202.1 km standard single-mode fiber (SSMF) link, consisting of four approximately 50 km fiber spans, was used as the sensing medium. Two optical carriers at wavelengths $\lambda_1 = 1549.72\ nm$ and $\lambda_2 = 1550.52nm$, optical power of 2 mW, and linewidth of 500 kHz, were launched from opposite ends of the fiber link and propagated in opposite directions. Wavelength-division multiplexer (WDM) is used to separate the light in different directions, and then a polarization analyzer (PA, Keysight N7781C) is used to continuously measure the state of polarization (SOP) of each transmitted optical carrier at the corresponding receiver. This bidirectional configuration provides two temporally related observations of the same perturbation and enables perturbation localization from their differential propagation delay.

Two narrow-linewidth optical sources were used to generate the counter-propagating sensing carriers. The optical powers were adjusted before launching the two carriers into the sensing fiber. A 60 m fiber section wound around a piezoelectric transducer (PZT, 91.67 nε/V) was used to introduce controlled dynamic perturbations at selected positions along the 202.1 km link. By relocating the perturbed section among different fiber spans, the response of the proposed method was evaluated at multiple longitudinal positions. The PZT was driven by sinusoidal electrical signals with adjustable frequency and amplitude, enabling controlled characterization of the frequency and strain responses.

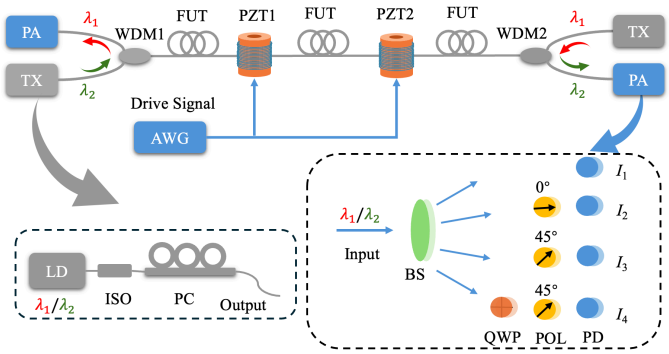


Fig. 2. Experiment setup for long-haul forward-transmission polarization-based distributed sensing over a 202.1 km standard single-mode fiber link. AWG: arbitrary waveform generator, TX: transmitter, RX: receiver, WDM1, WDM2: wavelength-division multiplexer, PZT: piezoelectric transducer, LD: laser diode, ISO: isolator, PC: polarization controller, OC: optical coupler, PA: polarization analyzer.

At the two receiving terminals, the transmitted SOPs were measured using two Keysight N7781C polarization analyzers. The analyzers provided the Stokes components $\boldsymbol{S}(t) = [S_1(t) \quad S_2(t) \quad S_3(t)]^T$ at a sampling rate of 1 MSa/s. The two analyzers were operated with a common external frequency reference and the same triggering signal to maintain a consistent time base between the two terminal measurements. For the following localization analysis, the longitudinal coordinate z is defined from the receiving terminal of λ_1, which is assigned as $z = 0$, while the opposite terminal is located at $z = L$, where L denotes the total fiber length. Accordingly, a perturbation

Authorized licensed use limited to: SHENZHEN UNIVERSITY. Downloaded on October 23,2026 at 04:14:54 UTC from IEEE Xplore. Restrictions apply.
© 2026 IEEE. All rights reserved, including rights for text and data mining and training of artificial intelligence and similar technologies. Personal use is permitted, but republication/redistribution requires IEEE permission. See https://www.ieee.org/publications/rights/index.html for more information.

This article has been accepted for publication in Journal of Lightwave Technology. This is the author's version which has not been fully edited and content may change prior to final publication. Citation information: DOI 10.1109/JLT.2026.3745673

occurring at position z is located at a propagation distance z from the λ_1 receiving terminal and $L-z$ from the λ_2 receiving terminal.

Since the two optical carriers propagate in opposite directions, the same perturbation-induced polarization variation reaches the two receiving terminals after different propagation times. For a perturbation occurring at position z, the corresponding propagation times are:

$$t_1 = \frac{z}{v_g}, t_2 = \frac{L-z}{v_g} \tag{20}$$

where $v_g = c/n_g$ is the optical group velocity in the sensing fiber and $n_g = 1.468$ is the corresponding group index. Defining the differential arrival time between the two terminal observations as $\Delta t = t_1 - t_2$, the longitudinal perturbation position can therefore be obtained as:

$$z = \frac{L + v_g \Delta t}{2} \tag{21}$$

In the experiment, the delay Δt is determined from the lag corresponding to the maximum normalized cross-correlation coefficient between the two terminal rotation-rate sequences. The lag search is restricted to -1.5 to +1.5 ms. No sub-sample peak interpolation or onset-envelope-based branch selection was applied. No additional fixed-delay calibration was applied to the reported localization results. The estimated differential delay is then substituted into Eq. 21 to determine the perturbation position. At the Stokes sampling rate of 1 MSa/s, the sampling interval is dt_s. A one-sample change in the estimated differential delay therefore corresponds to a nominal position increment of $\Delta z_s = v_g dt_s/2$. For standard SMF, this corresponds to approximately 100 m. In practice, fixed offsets can be calibrated using a reference perturbation at a known position, an optical/electrical timing marker, or a loop-back path. Long-term clock drift can be suppressed using GNSS-disciplined clocks, common 10 MHz references with 1 PPS (Pulse Per Second) triggers, or equivalent network-based synchronization. For dual-end configurations, factors such as finite sampling intervals, limited signal bandwidth, position-dependent signal-to-noise ratios, and asymmetric waveform distortion between the two propagation directions also contribute to time-delay errors.

IV. Stokes Rotation-Rate Extraction

The measured SOP traces are processed in the Stokes domain to extract perturbation-related rotation descriptor. The processing flow is shown in Fig. 3. First, each measured Stokes vector is normalized by its Euclidean norm to obtain a unit vector on the Poincaré sphere. This ensures that the subsequent averaging operates on polarization directions without weighting individual samples by their vector magnitudes. A centered 200 sample moving average is then applied independently to the three components to suppress measurement noise. Since component-wise averaging does not generally preserve the unit-norm constraint, the smoothed vectors are renormalized to unit length before calculating the rotation-rate descriptor. At a sampling rate of 1 MSa/s, the boxcar filter has its first spectral null at 5 kHz and a −3 dB bandwidth of approximately 2.2 kHz. The resulting normalized and filtered Stokes sequence is subsequently used for rotation-rate extraction.

Let $\boldsymbol{S}_{\lambda_i}(t)$ denote the normalized Stokes vector measured at wavelength λ_i. where i =1,2 represents the two counter-propagating measurements. The individual Stokes components describe the instantaneous SOP in the selected observation basis and therefore depend on the accumulated polarization transformation between the perturbation position and the observation terminal. Rather than directly using the absolute values of the individual Stokes components, the present method characterizes the angular evolution of the complete Stokes trajectory on the unit Poincaré sphere. Accordingly, the Stokes rotation rate is estimated from two consecutive terminal Stokes states separated by the sampling interval dt_s.

For time-domain waveform extraction, the scalar Stokes rotation rate is calculated directly from two adjacent normalized Stokes states as:

$$\omega_{rot,\ \lambda_i}(t) \cong \frac{\left\| \widehat{\boldsymbol{S}}_{\lambda_i}(n dt_s) \times \widehat{\boldsymbol{S}}_{\lambda_i}((n+1) dt_s) \right\|}{dt_s} \tag{22}$$

The rotation-rate descriptor is evaluated using a two-point forward-difference scheme based on two adjacent normalized Stokes states. The sampling interval $dt_s = 1\mu s$, and n denotes the discrete sample index. Thus, Eq. 22 is implemented using samples n and $n+1$, rather than a three-point central-difference approximation. It provides the discrete counterpart of the continuous Stokes rotation-rate descriptor introduced in Section II. It should be noted that the magnitude operation in Eq. 22 is nonlinear and may introduce DC and harmonic components for periodic Stokes trajectories. Therefore, for controlled multi-frequency perturbations, the physical excitation frequencies are identified and separated in the signed Stokes domain before evaluating the scalar rotation-rate magnitude.

Let θ_{λ_i} denote the angular separation between two adjacent normalized Stokes vectors. Since the magnitude of Eq. 22 is formally $\sin(\theta_{\lambda_i})/dt_s$, whereas the exact finite angular rate is θ_{λ_i}/dt_s. In the present measurements, the angular displacement between adjacent samples remains below 1 mrad. Under this condition, the small-angle approximation $\sin(\theta_{\lambda_i}) \cong \theta_{\lambda_i}$ is well satisfied, with a maximum relative approximation error below 1.67×10^{-7}. Consequently, Eq. 22 therefore provides an accurate discrete estimate of the Stokes rotation rate under the present experimental conditions.

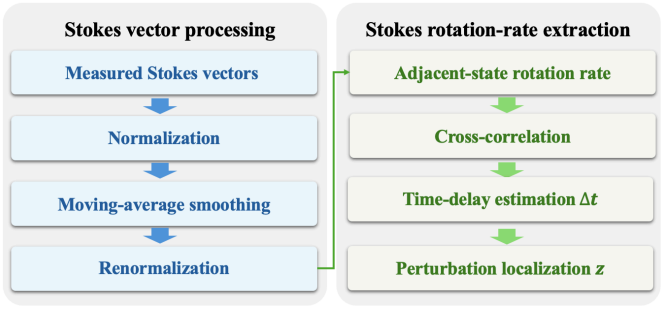


Fig. 3. Stokes-domain processing flow for extracting the scalar Stokes rotation-rate descriptor from the measured SOP traces.

The resulting $\omega_{rot,\ \lambda_i}(t)$ provides a scalar measure of the temporal motion of the measured SOP on the Poincaré sphere

Authorized licensed use limited to: SHENZHEN UNIVERSITY. Downloaded on October 23,2026 at 04:14:54 UTC from IEEE Xplore. Restrictions apply.
© 2026 IEEE. All rights reserved, including rights for text and data mining and training of artificial intelligence and similar technologies. Personal use is permitted, but republication/redistribution requires IEEE permission. See https://www.ieee.org/publications/rights/index.html for more information.

This article has been accepted for publication in Journal of Lightwave Technology. This is the author's version which has not been fully edited and content may change prior to final publication. Citation information: DOI 10.1109/JLT.2026.3745673

and is used as the sole polarization-dynamic descriptor in the following analysis. Compared with an individual Stokes component, it characterizes the angular motion of the complete normalized Stokes vector rather than its projection onto a single observation axis.

Fig. 4 presents a representative perturbation measurement obtained from the two receiving terminals. As shown in Fig. 4(a), the individual Stokes components measured at λ_1 and λ_2 exhibit different absolute trajectories since the perturbation-induced polarization variation experiences different accumulated polarization transformations before reaching the two observation terminals. After applying the processing procedure described above, the corresponding scalar rotation-rate waveforms are obtained, as shown in Fig. 4(b). Similar perturbation-induced temporal features can be identified in the two rotation-rate waveforms, together with a clear relative arrival-time difference.

Under perturbation-free conditions, the background rotation-rate levels at the two terminals are 62.63 rad/s and 17.32 rad/s, respectively. After background removal, the maximum perturbation responses reach 470.71 rad/s and 470.16 rad/s, respectively. Although the two terminal measurements exhibit different background levels and waveform details, the perturbation-induced temporal features are clearly retained in both rotation-rate sequences. This common temporal structure enables the relative arrival delay of the perturbation to be estimated from the two terminal measurements.

To provide a representative demonstration of dual-end localization, the relative delay between the two rotation-rate waveforms was estimated from the peak lag of their mean-removed cross-correlation and converted into longitudinal position using Eq. 21. For the example shown in Fig. 4(c), the perturbation was applied at a nominal position of 151.62 km. Over 64 repeated measurements, the mean estimated position was 151.35 km, with the Standard Deviation (STD) of 51.47 m, the Mean Absolute Error (MAE) of 273.03 m, and the Root Mean Squared Error (RMSE) of 277.76 m. This representative result demonstrates that the extracted Stokes rotation-rate waveform retains sufficient common temporal information at the two terminals for differential-delay-based localization.

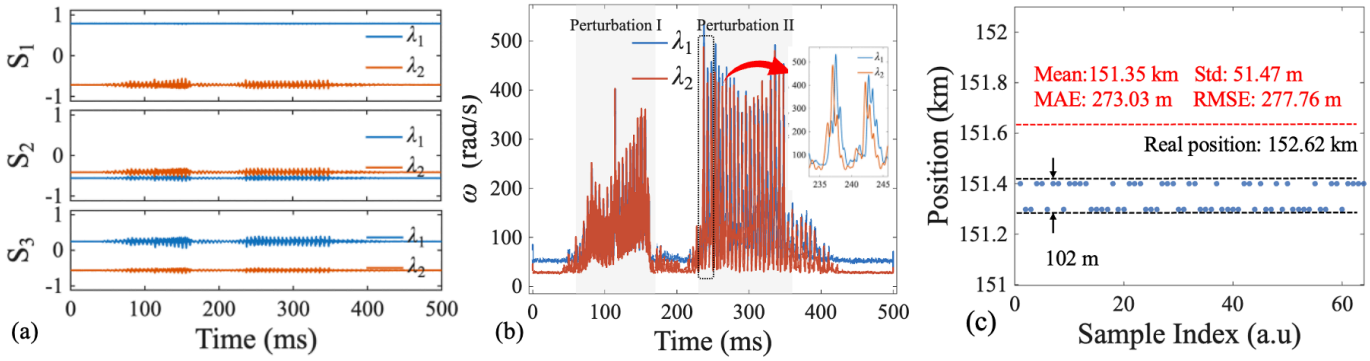


Fig. 4. Measured polarization responses: (a) Measured Stokes vector of λ_1, λ_2, (b) Perturbation rotation-rate magnitude $\|\boldsymbol{\omega}(t)\|$ of λ_1, λ_2, (c) repeated position estimates obtained from the rotation-magnitude waveform

V. Discussions

The experimental evaluation is organized in two stages. First, the dependence of different polarization observables on the physical launch SOP was quantitatively compared using the same raw Stokes measurements. This comparison was used to assess the consistency of the proposed Stokes rotation-rate descriptor under different polarization operating states. Based on these results, the scalar rotation rate ω was adopted as the sensing descriptor for the subsequent experiments. Its response characteristics were then evaluated with respect to perturbation position, excitation frequency, applied strain, dual-end localization, and simultaneous frequency-separated perturbations over the 202.1 km fiber link.

The invariance of ω to a static rotation of the Stokes observation coordinates, as established in Section II, should be distinguished from its dependence on the physical launch SOP. A change in the launch SOP changes the actual Stokes trajectory propagating through the fiber and can therefore modify the observable perturbation response. To experimentally quantify this dependence, six representative launch states, H, V, D, A, R, and L, distributed over the Poincaré sphere were tested at 1550.52 nm in the forward-propagation direction under the same perturbation condition (a 400 Hz sinusoidal perturbation applied at 202.1 km). For each SOP, we used the same raw Stokes measurements and, under the same acquisition and preprocessing conditions, calculated different polarization observable responses, primarily including the three components of the Stokes vector, azimuth ($\psi = atan2(S_2, S_1)$), polarization ellipticity ($\chi = arcsin(S_3)/2$), polarization angle (Jones-space amplitude-mixing angle, $\alpha = arccos(S_1)/2$), phase difference ($\phi = atan2(S_3, S_2)$), and the Stokes rotation-rate descriptor (ω).

For the controlled single-frequency measurements, the response of each conventional polarization observable was obtained by least-squares harmonic fitting at the known excitation frequency. For the rotation-rate descriptor, the three signed Stokes components were fitted simultaneously using a common sinusoidal model. The resulting cosine and sine coefficient vectors describe the harmonic Stokes trajectory and were assembled into a 3×2 coefficient matrix. Singular-value decomposition of this matrix was then used to obtain the two principal amplitudes of the fitted Stokes trajectory, from which the angular-rate response was calculated. This quantity represents the angular speed associated with the fitted single-frequency Stokes motion and is consistent with the instantaneous rotation-rate definition in Section II and the discrete estimator in Eq. 22. This harmonic-domain estimator is

Authorized licensed use limited to: SHENZHEN UNIVERSITY. Downloaded on October 23,2026 at 04:14:54 UTC from IEEE Xplore. Restrictions apply.
© 2026 IEEE. All rights reserved, including rights for text and data mining and training of artificial intelligence and similar technologies. Personal use is permitted, but republication/redistribution requires IEEE permission. See https://www.ieee.org/publications/rights/index.html for more information.

This article has been accepted for publication in Journal of Lightwave Technology. This is the author's version which has not been fully edited and content may change prior to final publication. Citation information: DOI 10.1109/JLT.2026.3745673

used for controlled single-frequency measurements since it directly quantifies the response at the known excitation frequency while avoiding the spectral ambiguity introduced by the nonlinear scalar-magnitude operation. The atan2-based quantities ψ and ϕ were unwrapped before harmonic fitting, while a fitted constant offset accounted for the static background without additional background subtraction.

For all controlled single-frequency measurements in the following analysis, the response magnitude was evaluated from the fitted harmonic Stokes trajectory using the same procedure described above. Table I summarizes the measured response amplitudes for the six launch SOPs (32 repeated measurements, each spanning 0.5 s). Each value in Table I represents the mean of 32 repeated measurements. The relative standard deviation of the rotation-rate response over the 32 repeated measurements remained within 0.0051%–0.0252%. The conventional polarization observables exhibit pronounced state-dependent variations. Depending on the launch state, a particular Stokes component or polarization-angle observable can show either a strong or a substantially reduced perturbation response since the measured SOP evolution is projected differently onto the corresponding observation coordinate. In comparison, the measured ω responses range from 198.72 to 300.68 rad/s over the six tested states. Thus, the rotation-rate descriptor is not strictly invariant to a physical change of the launch SOP, but its response variation is considerably smaller than that of the individual conventional polarization observables.

The corresponding detection signal-to-noise ratio (SNR) are compared in Fig. 5. The SNR was evaluated using the 400 Hz harmonic response as the signal contribution, while the remaining AC power within 0–5 kHz, excluding DC and the fitted signal contribution, was treated as background noise. For the rotation-rate descriptor, the harmonic response was evaluated from the signed Stokes representation before the scalar magnitude operation. Signal and noise powers were averaged over 32 repeated measurements before calculating the reported SNR, with the error bars indicating the repeat-to-repeat variability. The conventional observables exhibit large SNR variations among the six launch SOPs: an individual observable can provide a high SNR for one operating state while becoming substantially weaker for another. In contrast, the SNR of ω remains between approximately 20.66 and 22.09 dB over the six tested states, corresponding to a variation of only 1.43 dB. It should be emphasized that ω does not necessarily provide the highest SNR for every individual launch state. Rather, its principal advantage is the substantially more consistent detection performance obtained when the physical launch SOP is changed. To further quantify the launch-state dependence, the coefficient of variation (CV) is defined as:

$$CV = \frac{\delta}{\mu} \times 100\% \tag{23}$$

where μ and δ denote the mean and standard deviation, respectively, of the measured response amplitudes over the six launch SOPs. As summarized in Table II, the CV of ω is 17.01%, whereas the conventional polarization observables exhibit CVs ranging from 61.46% to 117.92%. These results quantitatively demonstrate that the rotation-rate representation substantially reduces, although does not eliminate, the dependence of the measured perturbation response on the physical launch SOP.

Long-term measurements were additionally used to characterize the time-varying SOP drift of the link. The terminal SOPs were recorded at 10 Hz over 10 h. The long-term drift was evaluated as the angular distance between each measured SOP and the initial SOP, whereas the short-term variation was evaluated as the angular distance between SOPs separated by 0.5 s. During a representative 10 h observation, the maximum angular deviations of the two terminal SOPs from their respective initial states reached approximately 127° and 169°, confirming appreciable long-term polarization evolution. In contrast, the median SOP changes over a 0.5 s interval were only approximately 0.023° and 0.024°, respectively, with 95% of the changes remaining below approximately 0.06°. Therefore, although the polarization operating state can evolve substantially over long timescales, it remains approximately quasi-static within the 0.5 s interval used for the subsequent localization measurements.

The long-term observation characterizes the SOP background evolution during the reported experiment, while the six-state comparison shows that ω provides substantially reduced launch-SOP dependence and more consistent sensing performance than the conventional polarization observables tested here. Accordingly, ω is used as the sole descriptor for sensing in the following experiments.

Table I. 400 Hz responses of different parameters for different SOP

SOP	S_1	S_2	S_3	$\psi\ (rad)$	$\chi\ (rad)$	$\alpha\ (rad)$	$\phi\ (rad)$	$\omega\ (rad/s)$
H	0.0103	0.1240	0.0296	0.0623	0.0148	0.0431	1.1470	227.23
V	0.0034	0.1269	0.0241	0.0638	0.0121	0.0130	1.1320	229.68
D	0.1202	0.0176	0.1178	0.0612	0.0592	0.0604	0.1200	300.68
A	0.1112	0.0187	0.1164	0.0566	0.0595	0.0557	0.1187	288.01
R	0.0240	0.1181	0.0075	0.6868	0.0356	0.0120	0.1185	214.52
L	0.0159	0.1107	0.0013	0.5420	0.0053	0.0080	0.1112	198.72

Authorized licensed use limited to: SHENZHEN UNIVERSITY. Downloaded on October 23,2026 at 04:14:54 UTC from IEEE Xplore. Restrictions apply.
© 2026 IEEE. All rights reserved, including rights for text and data mining and training of artificial intelligence and similar technologies. Personal use is permitted, but republication/redistribution requires IEEE permission. See https://www.ieee.org/publications/rights/index.html for more information.

This article has been accepted for publication in Journal of Lightwave Technology. This is the author's version which has not been fully edited and content may change prior to final publication. Citation information: DOI 10.1109/JLT.2026.3745673

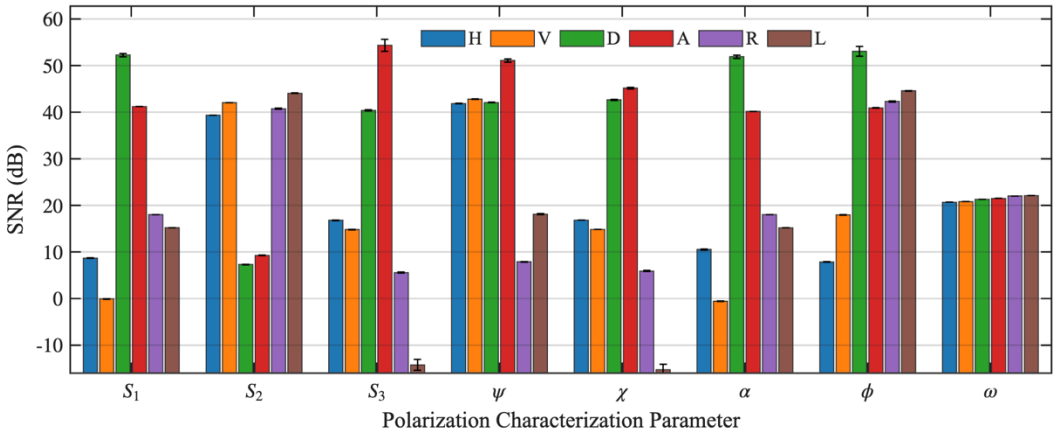


Fig. 5. Comparison of the response SNRs of different polarization observables under six launch SOPs

Table II. CV of different parameter responses across SOP

Parameter	Mean	Standard deviation	CV (%)
S_1	0.0475	0.0533	112.24
S_2	0.0860	0.0528	61.46
S_3	0.0494	0.0534	108.09
$\psi\ (rad)$	0.2454	0.2894	117.92
$\chi\ (rad)$	0.0311	0.0241	77.57
$\alpha\ (rad)$	0.0320	0.0238	74.30
$\phi\ (rad)$	0.4579	0.5280	115.31
$\omega\ (rad/s)$	243.14	41.36	17.01

After confirming the reduced emission polarization state dependence of ω through six-state comparison, its sensing characteristics were then evaluated as a function of perturbation location and excitation frequency. In the frequency response measurement, two orthogonal emission polarization states, H and V (i.e., X and Y), were selected as representative operating conditions. The purpose of choosing these two polarization states was not to replicate comprehensive emission polarization state robustness testing, but rather to verify whether the frequency-dependent response trend of the selected descriptor remained unchanged under different polarization inputs.

First, under the same driving conditions, a sinusoidal perturbation of 400 Hz was applied at different locations along a 202.1 km fiber link. As shown in Fig. 6(a), measurable rotational rate responses were obtained at all test locations for both backpropagation wavelengths. For λ_1, the measured response values were approximately 140 to 330 rad/s; while for λ_2, the values were approximately 150 to 220 rad/s. The results indicate that the polarization dynamics caused by the perturbation can be detected by the scalar rotational rate descriptor throughout the entire test link. Due to the inherent dispersion of the fiber, the response amplitude is not spatially uniform even under nominally identical excitation. This phenomenon is expected since the terminal polarization response depends not only on the local perturbation but also on the cumulative polarization transformation before and after the perturbation segment. As described in Section II in the long-distance transmission model, perturbations occurring at different longitude locations undergo different cumulative Jones transformations before reaching the observation terminal. Therefore, the absolute value of ω should be interpreted as the terminal observable under the corresponding link conditions, rather than a direct estimate of microscopic local fiber parameters.

Fig. 6(b) and 6(c) show the rotational rate responses of λ_1 and λ_2 as a function of excitation frequencies (1, 10, 100, 500, 1000 Hz), respectively. Both the frequency and rotational rate axes are plotted on logarithmic scales to cover a response range of several orders of magnitude. For both wavelengths, the rotational rate ω_0 monotonically increases from 1 Hz to 1 kHz. More importantly, the X-polarized and Y-polarized responses remain highly consistent throughout the studied frequency range, indicating that the overall frequency-dependent response trend is well maintained for these two typical emission states.

Fig. 6(b) and 6(c) show the frequency-dependent responses of ω under the same PZT driving-voltage condition. For both wavelengths, the measured rotation-rate response increases markedly as the excitation frequency is increased from 1 Hz to 1 kHz, while the X- and Y-polarized results remain closely matched over the investigated frequency range. This behavior is consistent with the definition of ω as the instantaneous angular speed of the measured Stokes trajectory. For perturbations producing comparable SOP excursions, a higher vibration frequency corresponds to a faster temporal evolution of the SOP and therefore gives a larger rotation-rate response.

This characteristic also indicates that the rotation-rate descriptor intrinsically emphasizes rapid temporal polarization variations. It is therefore particularly suitable for representing dynamic perturbations that induce relatively large instantaneous SOP changes, such as vibration and other rapidly varying disturbances. Conversely, slowly varying polarization changes produce smaller values of ω, since the same or comparable SOP excursion is distributed over a longer time scale. The descriptor consequently has reduced sensitivity to slowly varying perturbations, which represents an inherent limitation when very-low-frequency or quasi-static variations are of interest.

The absolute responses measured at λ_1 and λ_2 are also different, particularly at higher excitation frequencies. This

Authorized licensed use limited to: SHENZHEN UNIVERSITY. Downloaded on October 23,2026 at 04:14:54 UTC from IEEE Xplore. Restrictions apply.
© 2026 IEEE. All rights reserved, including rights for text and data mining and training of artificial intelligence and similar technologies. Personal use is permitted, but republication/redistribution requires IEEE permission. See https://www.ieee.org/publications/rights/index.html for more information.

This article has been accepted for publication in Journal of Lightwave Technology. This is the author's version which has not been fully edited and content may change prior to final publication. Citation information: DOI 10.1109/JLT.2026.3745673

behavior is consistent with the wavelength-dependent accumulated polarization transformation of the 202.1 km link. The two counter-propagating carriers therefore map the same local perturbation onto different terminal Stokes trajectories. Such wavelength-dependent response amplitudes should be taken into account through calibration when quantitative perturbation measurements are required.

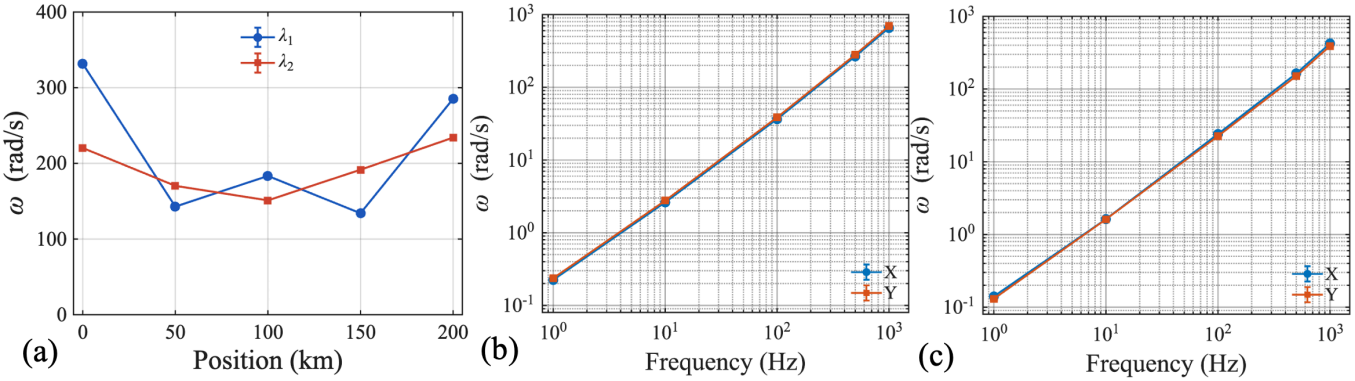


Fig. 6. Descriptor responses under perturbations at different positions and frequencies along the 202.1 km link: (a) Response at different perturbation locations, frequency-dependent response under X and Y input polarization states for (b) λ_1, and (c) λ_2.

The capability of the rotation-rate descriptor to quantitatively characterize perturbation strength was further evaluated by varying the strain applied to the PZT while maintaining the perturbation position and excitation frequency. The excitation frequency was fixed at 400 Hz throughout the strain-response measurement. Fig. 7 shows the measured ω as a function of applied strain for both operating wavelengths and the two tested input polarization states.

For λ_1, the fitted strain sensitivities are 346.88 and 368.15 rad·s^{-1}·με^{-1} for the X- and Y-polarized inputs, respectively. The corresponding coefficients of determination are R^2=1.0000 and 0.9999. For λ_2, the fitted sensitivities decrease to 232.51 and 205.75 rad·s^{-1}·με^{-1}, with R^2=0.9998 for both input polarization states. These results demonstrate a highly linear relationship between the measured rotation-rate response and the applied strain over the investigated range.

The fitted sensitivities retain a finite dependence on both the operating wavelength and the physical launch state. The sensitivity difference between the X- and Y-polarized measurements is approximately 6.1% at λ_1 and 12.3% at λ_2. In addition, the sensitivity at λ_2 is lower than that at λ_1, by approximately 33% for the X-polarized case and 44% for the Y-polarized case. These observations are consistent with the launch-SOP and wavelength dependence discussed above: the rotation-rate representation reduces the variation associated with the polarization operating state but does not remove the physical dependence of the terminal response on the accumulated polarization transfer. Quantitative strain measurements therefore require calibration under the corresponding link condition. The strain limit of detection (LoD) was estimated as:

$$LoD = \frac{3.3\sigma}{K} \tag{24}$$

where σ is the standard deviation of the rotation-rate trace over a perturbation-free 0.5-s interval, representing the overall background fluctuation about its finite mean, and K is the fitted strain sensitivity. The corresponding σ values are 0.8083, 1.1904, 1.2929, and 1.0911 rad/s for the λ_1:X, λ_1:Y, λ_2:X, and λ_2 :Y cases, respectively. Since σ represents an output fluctuation in rad/s and K relates strain to the same angular-rate response, σ/K gives the corresponding equivalent strain noise. The resulting LoDs are 7.69 and 10.67 nε for the X- and Y-polarized measurements at λ_1, respectively, and 18.35 and 17.50 nε at λ_2.

Overall, the strain measurements demonstrate that ω is not only suitable for detecting dynamic perturbations but can also provide quantitative information on perturbation strength after calibration. The high linearity is preserved under the tested operating conditions, while the remaining wavelength- and launch-state-dependent sensitivity reflects the accumulated polarization transfer of the long-haul link.

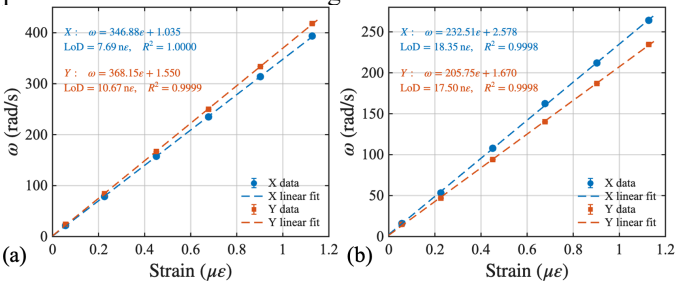


Fig. 7. Strain-dependent descriptor responses under X and Y input polarization states for: (a) λ_1, and (b) λ_2.

Having characterized the amplitude response of ω, we next examined whether the descriptor preserves the temporal information required for dual-end delay localization. The perturbation position was determined from the relative delay between the two terminal rotation-rate waveforms using the cross-correlation procedure and the position relation given in Eq. 21.

At five locations along the 202.1 km link, 64 repeated experiments were conducted to determine single-point localization under a 400 Hz sinusoidal perturbation, with each estimate obtained from a 0.5 s rotation rate sequence. As summarized in Table III, the nominal perturbation positions were 0.021, 50.61, 100.91, 151.62, and 202.05 km, whereas the corresponding mean estimated positions were 0.054, 50.47, 100.87, 151.72, and 201.55 km, respectively.

Authorized licensed use limited to: SHENZHEN UNIVERSITY. Downloaded on October 23,2026 at 04:14:54 UTC from IEEE Xplore. Restrictions apply.
© 2026 IEEE. All rights reserved, including rights for text and data mining and training of artificial intelligence and similar technologies. Personal use is permitted, but republication/redistribution requires IEEE permission. See https://www.ieee.org/publications/rights/index.html for more information.

This article has been accepted for publication in Journal of Lightwave Technology. This is the author's version which has not been fully edited and content may change prior to final publication. Citation information: DOI 10.1109/JLT.2026.3745673

The localization RMSE ranges from 67.44 to 498.53 m over the five tested positions. The minimum RMSE of 67.44 m is obtained at 100.91 km. At the 202.05 km position, the STD remains relatively small at 41.04 m, whereas the MAE and RMSE increase to 496.85 and 498.53 m, respectively. This combination of a small measurement-to-measurement spread and a larger absolute error indicates that the degradation near this position is dominated primarily by a systematic position bias rather than random localization fluctuation.

The position-dependent localization error can originate from residual synchronization offset, uncertainty in the effective group velocity, the finite 1 MSa/s Stokes sampling interval, limited signal bandwidth, position-dependent SNR, and asymmetric waveform distortion between the two terminal measurements. In particular, the counter-propagating optical carriers experience different accumulated polarization transformations before reaching their respective analyzers. Their terminal rotation-rate waveforms are therefore not expected to be perfectly identical, which can broaden or shift the cross-correlation peak and introduce a position-dependent delay bias. Nevertheless, the results demonstrate that the scalar rotation-rate waveform retains sufficient common temporal information at the two terminals for differential-delay-based perturbation localization.

Table III. Vibration localization accuracy obtained using the Stokes rotation-rate descriptor

Actual position (km)	0.021	50.61	100.91	151.62	202.05
Mean position (km)	0.054	50.47	100.87	151.72	201.55
STD (m)	78.78	72.93	52.25	71.08	41.04
MAE (m)	73.54	143.45	55.07	105.30	496.85
RMSE (m)	85.18	159.01	67.44	122.12	498.53

Finally, a proof-of-concept dual-event experiment was performed to examine whether simultaneous perturbations occupying different frequency bands could be separated and localized. Two sinusoidal perturbations at 150 and 200 Hz were applied at different longitudinal positions. Since the scalar rotation-rate magnitude is nonlinear, the physical perturbation frequencies were first identified in the signed Stokes domain before the magnitude operation. Specifically, a joint Stokes spectrum was constructed by taking the root-sum-square of the spectral amplitudes of the three signed Stokes components, thereby representing the overall three-dimensional Stokes response without relying on any individual Stokes projection. As shown in Fig. 8(a), the joint Stokes spectrum exhibits distinct components at 150 and 200 Hz at both receiving terminals. The two perturbation components were then separated in the signed Stokes domain using zero-phase band-pass filters (BPF) of 140–160 Hz and 190–210 Hz, respectively. For each separated branch, the filtered Stokes variation was combined with the corresponding local mean SOP and renormalized to the unit Poincaré sphere. The scalar rotation-rate waveform was subsequently calculated using Eq. 22. The two resulting rotation-rate responses are shown in Fig. 8(a), demonstrating that the 150 and 200 Hz perturbations can be independently recovered before the dual-end delay estimation.

The corresponding separated rotation-rate waveforms were then used for the same cross-correlation-based localization procedure described above. As shown in Fig. 8(b), the 150 Hz component is localized at a mean position of 100.90 km, with an STD of 325.52 m, an MAE of 260.35 m, and an RMSE of 320.61 m. The 200 Hz component is localized at a mean position of 52.95 km, with an STD of 160.04 m, an MAE of 2340.14 m, and an RMSE of 2345.43 m. These results demonstrate that two simultaneous perturbations occupying different frequency components can be distinguished and associated with different regions of the fiber link. The localization accuracy is nevertheless degraded compared with the single-event measurements, particularly for the 200 Hz component.

The present experiment should therefore be regarded as a proof-of-concept demonstration of frequency-separated dual-event discrimination, rather than a general solution for simultaneous multi-event localization. The increased error can arise from waveform superposition, unequal perturbation amplitudes, direction-dependent polarization transfer, reduced similarity between the two terminal waveforms, and residual uncertainty in the delay estimation. Perturbations overlapping in both time and frequency would require additional signal-separation or estimation techniques and are beyond the scope of the present work.

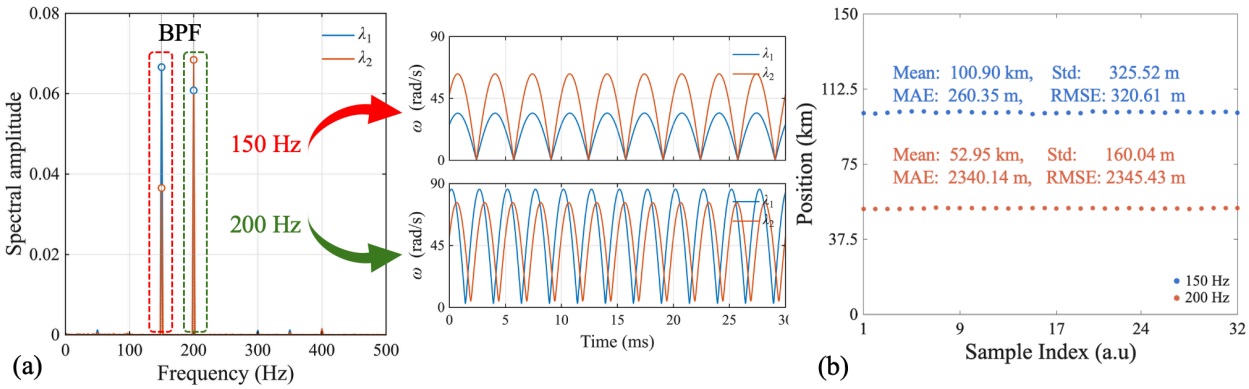


Fig. 8. Dual-event separation in the signed Stokes domain and subsequent localization using the Stokes rotation-rate descriptor: (a) Signed-Stokes frequency separation and corresponding rotation-rate responses, (b) Localization results of the separated dual events.

Authorized licensed use limited to: SHENZHEN UNIVERSITY. Downloaded on October 23,2026 at 04:14:54 UTC from IEEE Xplore. Restrictions apply.
© 2026 IEEE. All rights reserved, including rights for text and data mining and training of artificial intelligence and similar technologies. Personal use is permitted, but republication/redistribution requires IEEE permission. See https://www.ieee.org/publications/rights/index.html for more information.

This article has been accepted for publication in Journal of Lightwave Technology. This is the author's version which has not been fully edited and content may change prior to final publication. Citation information: DOI 10.1109/JLT.2026.3745673

VI. Conclusion

A scalar Stokes rotation-rate descriptor has been employed and experimentally evaluated for long-haul forward-transmission polarization-based distributed sensing over a 202.1 km standard single-mode fiber link. Measurements under six representative launch SOPs show an across-state coefficient of variation of 17.01%, compared with 61.46%–117.92% for conventional polarization observables, while the detection SNR varies by only 1.43 dB. The descriptor also exhibits highly linear strain responses with R^2>0.9998 and enables single-event localization with RMSEs of 67.4-498.5 m over five tested positions. Frequency-separated dual-event detection is further demonstrated as a proof of concept. These results establish the Stokes rotation rate as a compact and comparatively launch-SOP-consistent representation for dynamic perturbation sensing over long-haul forward-transmission fiber links, while very slow or quasi-static variations remain a limitation of the rate-based formulation.

Disclosures

The authors declare no conflicts of interest.

References

[1] G. Marra, C. Clivati, R. Luckett, A. Tampellini, J. Kronjäger, L. Wright, A. Mura, F. Levi, S. Robinson, A. Xuereb, B. Baptie, and D. Calonico, "Ultrastable laser interferometry for earthquake detection with terrestrial and submarine cables," *Science,* vol. 361, no. 6401, pp. 486-+, Aug 3, 2018.

[2] G. Marra, D. M. Fairweather, V. Kamalov, P. Gaynor, M. Cantono, S. Mulholland, B. Baptie, J. C. Castellanos, G. Vagenas, J. O. Gaudron, J. Kronjäger, I. R. Hill, M. Schioppo, I. B. Edreira, K. A. Burrows, C. Clivati, D. Calonico, and A. Curtis, "Optical interferometry-based array of seafloor environmental sensors using a transoceanic submarine cable," *Science,* vol. 376, no. 6595, pp. 874-+, May 20, 2022.

[3] Z. Zhan, M. Cantono, V. Kamalov, A. Mecozzi, R. Müller, S. Yin, and J. C. Castellanos, "Optical polarization-based seismic and water wave sensing on transoceanic cables," Science, vol. 371, no. 6532, pp. 931–936, Feb. 2021.

[4] J.-T. Li, B. Chang, J.-T. Du, T. Tan, Y. Geng, H. Zhou, Y.-P. Liang, H. Zhang, G.-F. Yan, L.-M. Ma, Z.-L. Ran, Z.-N. Wang, B.-C. Yao, and Y.-J. Rao, "Coherently parallel fiber-optic distributed acoustic sensing using dual Kerr soliton microcombs," Sci. Adv., vol. 10, no. 3, Art. no. eadf8666, Jan. 2024.

[5] L. Costa, S. Varughese, P. Mertz, V. Kamalov, and Z. Zhan, "Localization of seismic waves with submarine fiber optics using polarization-only measurements," Commun. Eng., vol. 2, Art. no. 67, Oct. 2023.

[6] A. Mecozzi, M. Cantono, J. C. Castellanos, V. Kamalov, R. Muller, and Z. Zhan, "Polarization sensing using submarine optical cables," Optica, vol. 8, no. 6, pp. 788–795, Jun. 2021.

[7] J. Fang, M.-F. Huang, S. Kotrla, T. J. Xia, G. A. Wellbrock, J. A. Mundt, T. Wang, and Y. Aono, "Field trial of high-sensitivity forward-transmission sensing for real-world event detection over live urban fiber networks," J. Lightwave Technol., vol. 44, no. 3, pp. 1167–1177, 2026.

[8] J. Liu, H. Li, H. Y. Noh, P. Santi, B. Biondi, and C. Ratti, "Urban sensing using existing fiber-optic networks," Nat. Commun., vol. 16, Art. no. 3091, 2025.

[9] J. Tang, X. Li, C. Cheng, Y. Hao, B. Yang, J. Li, Z. He, Y. Yang, and W. Hu, "Forward-transmission based distributed fiber sensing compatible with C+L unidirectional communication systems," in Proc. Optical Fiber Communication Conf. (OFC), 2024, paper M1K.3.

[10] A. Mecozzi, C. Antonelli, M. Mazur, N. Fontaine, H. Chen, L. Dallachiesa, and R. Ryf, "Use of optical coherent detection for environmental sensing," J. Lightwave Technol., vol. 41, no. 11, pp. 3350–3357, Jun. 2023.

[11] H. Zhong, Z. Peng, Y. Kong, G. Chen, Y. Meng, Y. Shi, W. Liang, S. Xiao, R. Shan, Z. Zhang, C. Liao, J. He, C. Fu, and Y. Wang, "High-spatial-resolution quasi-distributed acoustic sensing with phase noise suppression based on φ-OFDR," Opt. Express, vol. 32, no. 20, pp. 35975–35984, Sep. 2024.

[12] X. Pan, K. Cui, A. Zheng, Z. Ren, J. Ma, and R. Zhu, "Fading suppression method based on redundant data within the spatial resolution and deep learning for a Φ-OTDR system," Opt. Express, vol. 33, no. 9, pp. 18642–18658, Apr. 2025.

[13] M. Soriano-Amat, H. F. Martins, V. Durán, L. Costa, S. Martin-Lopez, M. Gonzalez-Herraez, and M. R. Fernández-Ruiz, "Time-expanded phase-sensitive optical time-domain reflectometry," Light Sci. Appl., vol. 10, no. 1, Art. no. 51, Mar. 2021.

[14] A. Mecozzi, "Sensing with submarine optical cables," APL Photon., vol. 9, no. 7, Art. no. 070902, Jul. 2024.

[15] S. Pellegrini, L. Minelli, L. Andrenacci, G. Rizzelli, D. Pilori, G. Bosco, L. Della Chiesa, C. Crognale, S. Piciaccia, and R. Gaudino, "Overview on the state of polarization sensing: application scenarios and anomaly detection algorithms," J. Opt. Commun. Netw., vol. 17, no. 2, pp. A196–A209, Feb. 2025.

[16] A. Mecozzi, C. Antonelli, A. Marullo, D. Decaroli, L. Palmieri, L. Schenato, S. Varughese, P. Mertz, and A. Napoli, "Geophysical sensing using Jones matrices extracted from submarine optical cable transceivers carrying live traffic," Optica, vol. 12, no. 11, pp. 1712–1719, Nov. 2025.

[17] J. P. Gordon and H. Kogelnik, "PMD fundamentals: Polarization mode dispersion in optical fibers," Proc. Natl. Acad. Sci. U.S.A., vol. 97, no. 9, pp. 4541–4550, Apr. 2000.

[18] C. J. Carver and X. Zhou, "Polarization sensing of network health and seismic activity over a live terrestrial fiber-optic cable," Commun. Eng., vol. 3, Art. no. 91, 2024, doi: 10.1038/s44172-024-00237-w.

[19] G. P. Agrawal, Nonlinear Fiber Optics, 6th ed. Amsterdam, The Netherlands: Elsevier, 2019.

[20] D. H. Goldstein, Polarized Light, 3rd ed. Boca Raton, FL, USA: CRC Press, 2011.

[21] S. Li, "Jones-matrix analysis with Pauli matrices: Application to ellipsometry," J. Opt. Soc. Amer. A, vol. 17, no. 5, pp. 920–926, May 2000.

Xing Rao was born in Jiangxi, China, in 1998. He received the B.S. degree in optoelectronic information science and engineering from Nanchang Hangkong University, Nanchang, China, in 2020, and the Ph.D. degree from Shenzhen University, Shenzhen, China, in 2025. He is currently a Postdoctoral Researcher at Shenzhen University. His current research interests focus on integrated sensing and communication.

George Y. Chen graduated with a 4-year MEng (Bachelor's and Master's joint degree) from Imperial College London in 2009, in the field of electronics and electrical engineering with computer science. He completed his PhD from the Optoelectronics Research Centre at the University of Southampton in 2013. He worked in an industrial research lab as a postdoctoral research fellow for SPI Lasers Ltd. from 2013 to 2015. He joined the University of South Australia as a research fellow in 2015, and senior research fellow in 2019. He was a part of the MinEx CRC. He joined Shenzhen University as a Professor in 2021. He is a Senior Member of Optica / IEEE.

Yiping Wang was born in Chongqing, China, in 1971. He received the B.Eng. degree in precision instrument engineering from Xi'an Institute of Technology, China, in 1995 and the M.S. degree and Ph.D. degree in optical engineering from Chongqing University, China, in 2000 and 2003, respectively. From 2003 to 2005, he was with Shanghai Jiao Tong University, China, as a Postdoctoral Fellow. From 2005 to 2007, he was with the Hong Kong Polytechnic University, as a Postdoctoral Fellow. From 2007 to 2009, he was with the Institute of Photonic Technology (IPHT), Jena, Germany, as a

Authorized licensed use limited to: SHENZHEN UNIVERSITY. Downloaded on October 23,2026 at 04:14:54 UTC from IEEE Xplore. Restrictions apply.
© 2026 IEEE. All rights reserved, including rights for text and data mining and training of artificial intelligence and similar technologies. Personal use is permitted, but republication/redistribution requires IEEE permission. See https://www.ieee.org/publications/rights/index.html for more information.

This article has been accepted for publication in Journal of Lightwave Technology. This is the author's version which has not been fully edited and content may change prior to final publication. Citation information: DOI 10.1109/JLT.2026.3745673

Humboldt Research Fellow. From 2009 to 2011, he was with the Optoelectronics Research Centre (ORC), University of Southampton, U.K., as a Marie Curie Fellow. Since 2012, he has been with Shenzhen University, Shenzhen, China, as a Distinguished Professor. His current research interests focus on optical fiber sensors, fiber gratings, and photonic crystal fibers. He has authored or coauthored 1 book, 21 patent applications, and more than 240 journal and conference papers. Prof. Wang is a Senior Member of IEEE, a Fellow of the Optica, and a Fellow of the Chinese Optical Society.

Authorized licensed use limited to: SHENZHEN UNIVERSITY. Downloaded on October 23,2026 at 04:14:54 UTC from IEEE Xplore. Restrictions apply.
© 2026 IEEE. All rights reserved, including rights for text and data mining and training of artificial intelligence and similar technologies. Personal use is permitted, but republication/redistribution requires IEEE permission. See https://www.ieee.org/publications/rights/index.html for more information.